Anisotropy of partial structure factors in an unmixed Cu-Ni-Fe single crystal studied by anomalous small-angle X-ray scattering

Anisotropy of partial structure factors in an unmixed Cu–Ni–Fe single crystal studied by anomalous small-angle x-ray scattering

O Lyon† and J P Simon‡

† Laboratoire d'Utilisation du Rayonnement Electromagnétique (CNRS), Bâtiment 209D, 91405 Orsay, France
‡ Laboratoire de Thermodynamique et Physico-chimie Métallurgiques, Ecole Nationale Supérieure d'Electrochimie et d'Electrométallurgie de Grenoble, Institut National Polytechnique de Grenoble, BP 75, 38402 Saint Martin d'Hères, France

Abstract. To study the anisotropy of phase separation in Cu–Ni–Fe alloys, small-angle x-ray scattering has been performed on a single-crystal foil. The 3D scattering pattern consists of an orientation-dependent ring. The intensity is a maximum along the $\langle 100 \rangle^*$ and a minimum along the $\langle 111 \rangle^*$ directions. The scattering is explained in terms of a non-interacting pile-up model of alternating Cu- and Ni–Fe-rich platelets along $\langle 100 \rangle$ directions. Moreover, the magnitude of the anomalous effect depends on the crystallographic orientation. The analysis shows that the two-phase description is insufficient to describe the derived PSFs. An interpretation is offered in terms of an interfacial segregation of Fe with a maximum amplitude in the plane of the $\{100\}$ platelets.

1. Introduction

The theories of phase separation, including the problems of metastability and instability, has received considerable attention in recent years (for reviews see Furukawa (1985) or Binder (1991)). Usually these theories apply to binary systems, although more recent calculations have extended spinodal decomposition to the case of multicomponent alloys (Hoyt 1989, 1990). For simplicity, several ternary alloys have been studied by small-angle neutron-scattering (SANS) or small-angle x-ray-scattering (SAXS) techniques as if they were pseudo-binaries, and in particular the Cu–Ni–Fe alloys (Wagner *et al* 1984). Moreover, these SANS and SAXS investigations have usually been performed on polycrystalline samples, and the results have been compared with isotropic models of phase separation. In Cu–Ni–Fe alloys, it is known from transmission electron microscopy (TEM) (Wahi and Stajer 1984) and from field ion microscopy (FIM) (Piller *et al* 1984) that the phase separation pattern is tweed like with a strong $\langle 100 \rangle$ anisotropy. To gather quantitative information on the anisotropy, one has to measure SANS and SAXS on single crystals, as for example in Al–Zn (Guilarducci de Salva *et al* 1987) or in other systems reviewed by Kostorz (1991).

Our previous investigation of polycrystalline Cu–Ni–Fe samples (Lyon and Simon 1987, hereafter referred to as I, Lyon and Simon 1988, hereafter referred to as II), confirmed that the phase separation follows the tie-line of the calculated phase

diagram (Chart *et al* 1982). The two-phase pattern consists of domains enriched in Ni and Fe alternating with Cu-rich domains, in agreement with the atom probe measurements of the solute concentration profile (Piller *et al* 1984). Since the bulk alloy composition corresponds to the centre of the miscibility gap, a surrounding phase and a surrounded phase cannot be unambiguously defined and a description in terms of 'precipitates and matrix' would be misleading. Moreover, the determination of the partial structure factors (PSFs) from anomalous SAXS data (I) showed that this two-phase description was only a rough first approximation; the PSFs are incompatible with simple phase separation with sharp interfaces. The PSFs (II) were decomposed into the two-phase term plus an extra contribution. Various models were discussed to explain the deviation (three-phase model, etc) and the most likely explanation was an enrichment of Fe at the interfaces between the coherent Cu-rich and Ni–Fe-rich domains.

For this reason, a single-crystal sample was made with the kind assistance of Mme Y Calvayrac of the Centre d'Etudes de Chimie Métallurgique CNRS Laboratory in Vitry sur Seine, in order to check any orientation dependence of the scattering spectra. To ensure that the PSFs were determined with as small an uncertainty as possible, we also developed a selection criterion of the best data set among the over-dimensioned anomalous measurements. This reduction criterion will be given in the appendix.

This paper first recalls the method for the determination of PSFs. This is followed by a description of the sample preparation and of the experimental conditions. The measured PSFs are described with emphasis on their dependence on crystallographic orientation. Their interpretation to a first approximation is given in terms of an anisotropic two-phase pattern and then the correction term is introduced and discussed in microstructural terms.

2. PSF determination

The scattering intensity for a ternary system is a linear combination of six PSFs, weighted by the atomic scattering factors f_i:

$$I(q, E) = \sum_{i,j=0}^{2} f_i(E) f_j^*(E) S_{ij}(q). \tag{1}$$

The complex f_i depend on the photon energy E but are independent of the reciprocal-lattice vector q at small angles. The PSF $S_{ij}(q)$ is simply the Fourier transform of the corresponding pair correlation function. In a crystalline alloy, three of the six PSFs are linearly independent. Thus, using $F_i = \|f_i - f_0\|$, where the index 0 stands for one of the elements, and defining φ as the angle between F_1 and F_2, equation (1) can be rewritten as

$$I_k(q, E_k) = F_1^2(E_k) S_{11}(q) + 2F_1(E_k) F_2(E_k) \cos \varphi(E_k) S_{12}(q) + F_2^2(E_k) S_{22}(q) \tag{2}$$

where I_k ($k = 1, \ldots, n$) is the intensity of the measurement taken at E_k.

Since the system of linear equations (2) is ill conditioned, we reduce its uncertainty by recording scattering profiles at n energies, typically ten values. The procedure used

to extract the three independent PSFs from this over-dimensioned linear system is the same as in I. However, a systematic procedure for data selection to minimize the uncertainty has been developed. This method, given in detail in the appendix, presents a compromise between the elimination of out-of-range data, i.e. incompatible data, and the ensuing loss in precision. The method is based on a graphical representation. The integral over q of equation (2) can be regarded as the scalar product of a vector $A(E)$ by an unknown vector $\langle S \rangle$:

$$\langle I_k(E_k) \rangle = A(E_k) \cdot \langle S \rangle \tag{3}$$

where the angular brackets denote the integrals over q. It has been shown (I) that the system of linear equations (3) is almost singular near one absorption edge and that it can yield only two parameters. We choose a representation of $\langle S_{11} \rangle$, $\langle S_{22} \rangle$ and $\langle S_{12} \rangle$ in an orthonormal 3D space and then the vectors $A(E_k)$ define a plane. Making a change in basis to principal axes defined by the mean direction of A, its perpendicular in the plane and the normal to the plane, all $\langle I(E_k) \rangle$, which are straight lines in the plane, should intersect at the same point. A figure of merit is defined such that at its lowest the condition of all lines intersecting at a single point is best satisfied. The set of scattering profiles giving the lowest relative dispersion for a given edge can then be selected graphically.

The reduction has to be performed without sacrificing the compatibility between edges. At this stage of the analysis, the components of $\langle S \rangle$ are known on each plane corresponding to the two edges. It is expected that their projections on the intersection of both planes should be common. The ratio of the projections provides an estimate of the compatibility between the two edges which, in practice, is found to be very good.

Finally, when the reduction has converged, the PSFs are computed for all wavevectors q by a least-squares method and a singular value decomposition algorithm to invert the corresponding matrix.

3. Sample preparation and experimental conditions

The alloy was prepared from 99.99% pure deoxidized metals by semilevitation under pure argon and chill cast in a copper ingot. The single crystals were obtained by a Bridgmann technique. Owing to the very slow solidification rate, the solidification structure is a large-scale dendritic pattern, which is tweed like along the $\langle 100 \rangle$ directions with a dendrite periodicity of about 0.1 mm. Nevertheless, since both the dendrites rich in Cu and the interdendritic zones rich in Ni–Fe are FCC, they are in epitaxial contact, constituting a single crystal which can then be homogenized by prolonged annealing near the melting point (1 week at 1150 °C in argon–hydrogen). After performing a Laue analysis for the orientation determination, slices of about 0.3 mm were cut with a diamond saw, mechanically thinned to 0.05–0.08 mm and finally electrochemically thinned to 0.025–0.015 mm to optimize the x-ray transmission measurements. The sample was rehomogenized for 1 h at 850 °C under vacuum to cause the small-scale heterogeneities which develop during the slow cooling from 1150° C to revert and then water quenched. Finally, the heat treatment for phase separation consisted of 4 h at 550 °C under high vacuum. The large-scale homogeneity was verified by x-ray analysis in the scanning electron microscope and the final composition was found to be $Cu_{0.441}Ni_{0.422}Fe_{0.137}$.

Anomalous SAXS experiments were performed on beam line D22 of the synchrotron radiation facility of the Laboratoire d'Utilisation du Rayonnement Electromagnétique (Orsay) equipped with a double monochromator (Ge_{111}) and a position-sensitive detector (PSD). The monochromator was calibrated by running absorption experiments through the Ni edge. Since the samples are weak x-ray scatterers, the complete beam line has to be under vacuum. A simple triple-axis sample holder was fitted to the sample changer.

The single crystal was oriented with the help of a two-dimensional PSD. However, since this detector has an insufficient spatial resolution, the scattering was recorded with a one-dimensional PSD. Scattering profiles were recorded near both the Fe and the Ni absorption edges (located at 7112 eV and 8333 eV, respectively). They were corrected to account for the sample thickness and transmission, for residual parasitic scattering, and for the position and energy dependence of the detector efficiency. Finally, the flat Fe fluorescence which, near the Ni edge, dominates the elastic signal at large q, was removed using the same procedure as in II. The intensity of this fluorescence allowed the determination of absolute efficiencies needed to express structure factors in absolute units.

4. Experimental results

Photographs of the SAXS pattern under three different crystallographic orientations, taken at 8322 eV to minimize the exposure time, are shown in figure 1.

(i) The scattering pattern from the [001] zone axis (figure 1(*a*)) shows a fourfold symmetry; it exhibits strong extended spots 100* located along the ⟨100⟩* directions. There is no evidence of an intensity maximum located at a position corresponding either to 200* or to 110*. Thus the structure is not expected to be modelled by a long-range periodic arrangement of precipitates.

(ii) Figure 1(*b*) shows the scattering pattern for an orientation near [011]. The photograph was overexposed to enhance the weaker 011* secondary maxima. Maxima along ⟨111⟩* directions are also present and are about three times weaker than the maxima along ⟨110⟩*. Thus the ⟨111⟩* orientations are the directions of the lowest saddle points in the halo that separates the origin of reciprocal space from large wavevectors. All saddle points are located at roughly the same wavenumber q, which confirms the absence of long-range periodicity of the pattern.

(iii) The last orientation investigated (figure 1(*c*)) is [111]. It shows the usual sixfold symmetry but with intensity maxima located along ⟨112⟩* directions and with saddle points in the ⟨110⟩* directions.

A 3D representation of the scattering is schematized in figure 2. In this figure, the maxima, located along ⟨100⟩*, are approximated by spheres; the interstices between three adjacent spheres present the highest intersphere distance in the ⟨111⟩* directions while the intersphere regions in the ⟨110⟩* directions are only saddle points.

In order to obtain more quantitative information on the scattering anisotropy, the (001)* plane was scanned by translating the one-dimensional PSD and the SAXS spectra was recorded at an energy of 7104 eV. Figure 3(*a*) shows the reconstructed isointensity map of the (001)* plane. Non-equidistant isointensity contours were chosen in order to emphasize the weak scattering along the ⟨110⟩* direction. As previously noted in figure 1(*a*), the high-intensity spots are located along the ⟨100⟩*
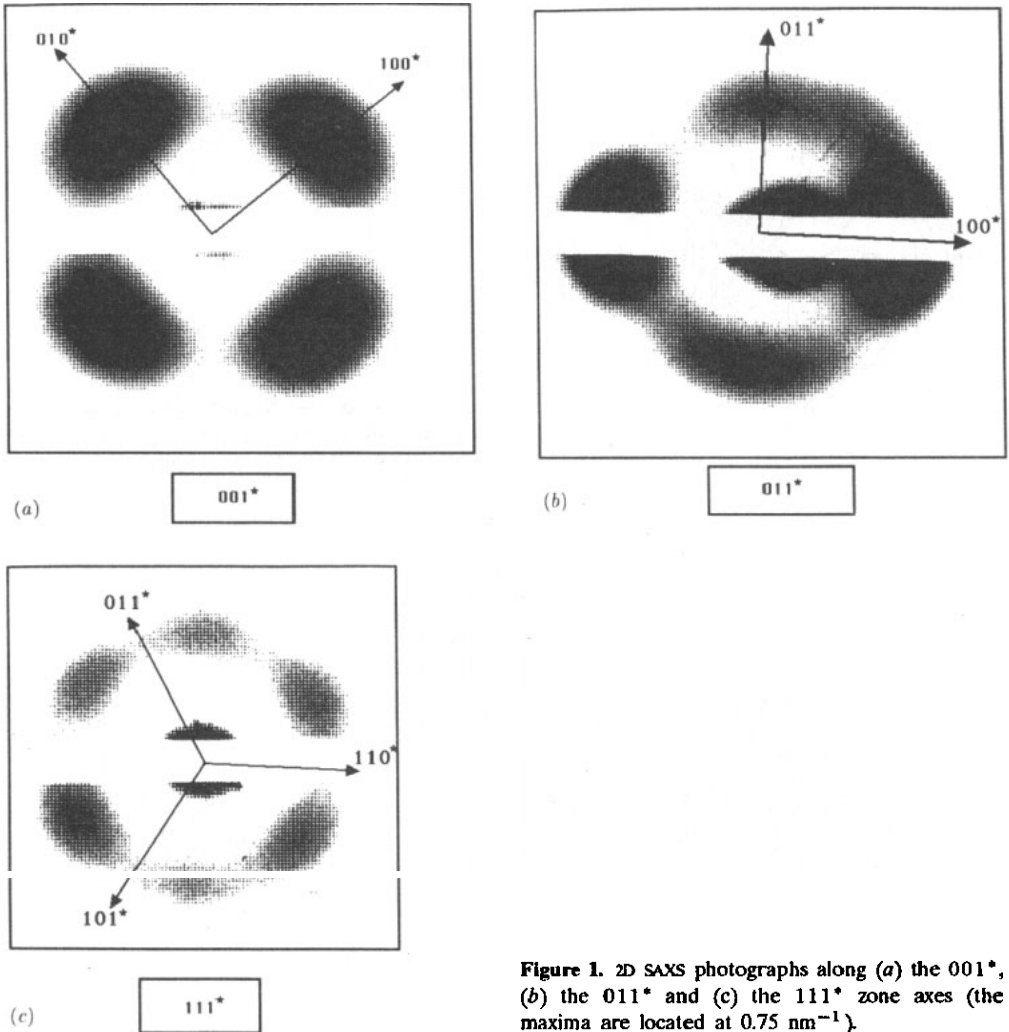
Figure 1. 2D SAXS photographs along (a) the 001*, (b) the 011* and (c) the 111* zone axes (the maxima are located at 0.75 nm^{-1}).

directions and the saddle points along the ⟨110⟩* directions. Figure 4 shows the ratio of the intensity of the local maximum to that of the 100* maximum as a function of the angle α between [100]* and the direction of observation in the (001)* plane (as shown in figure 3(a)). The right-hand side ordinate axis displays the corresponding relative position of the maximum. Both amplitude and position decrease as a function of α; along the [110]* saddle-point direction ($\alpha = 45°$), $I_{110*}/I_{100*} = 0.17$ and $q_{110*}/q_{100*} = 0.87$. The open symbols in this figure are calculated with the pile-up model described in section 5.

Next, directions were selected (figures 2 and 3(a)) for a more detailed study: the [100]* direction (OX), a direction along [010]* that passes through the centre of the 100* maximum (MY), a direction at 30° from OX (OB), and finally a direction along [110]* (OC).

For each direction, near both the Fe and the Ni absorption edges, scattering
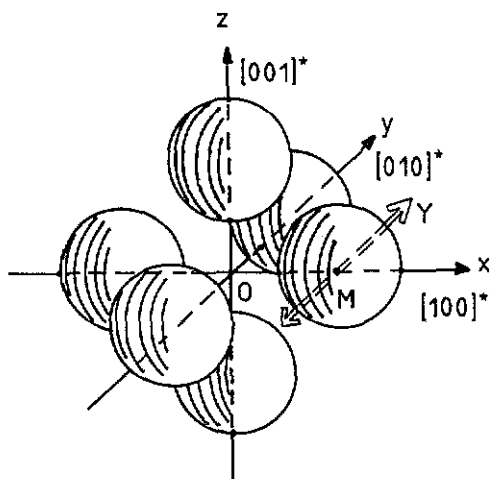
z

[001]*

[010]*

y

Y

x

O   M   [100]*

Figure 2. Schematic diagram of the 3D scattering pattern. The spheres represent the maxima and simulate the half-height isointensity surface.

contour number	relative intensity
1	0.033
2	0.067
3	0.1
4	0.133
5	0.166
6	0.2
7	0.3
8	0.4
9	0.6
10	0.8
11	0.9
(maxi)	1.0

100*

X
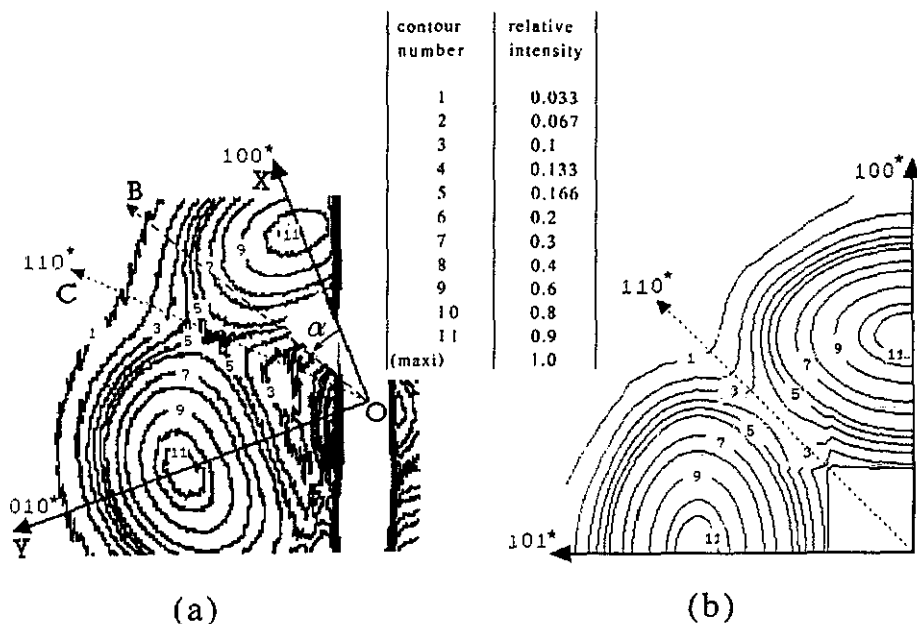
B

110*

C

α

O

010*

Y

(a)

100*

110*

101*

(b)

Figure 3. Isointensity contours of the SAXS in the (001)* reciprocal plane determined from (a) experiment and (b) the pile-up model (cf section 5).

patterns were recorded at five different photon energies. The shape and relative intensities along OX, OB and OC are similar to profiles for polycrystalline samples given in I and II. For this reason, we present here unusual anomalous MY patterns (figure 5). The reduction procedure described above was applied to the measured profiles.

The PSFs are given in figure 6. It can be seen that all the homoatomic PSFs (the three top curves) are positive, as they should be, and have very similar profiles with a hump, much like the measured scattering profiles themselves. For the PSFs in the
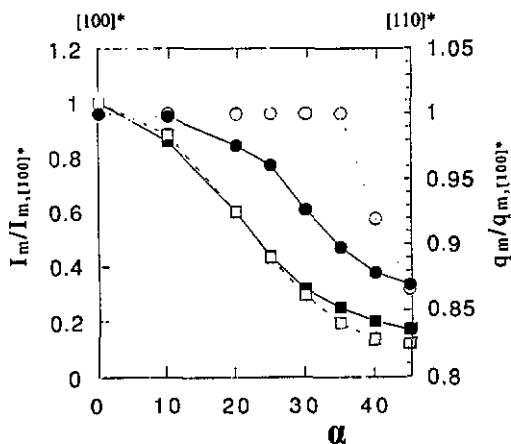
Figure 4. Relative intensity (■, □) and position (●, O) of the maximum as a function of the scattering direction in the $(001)^*$ plane: ■, ●, experimental measurements; □, O, values obtained with the pile-up model; lines are provided as a guide to the eye.
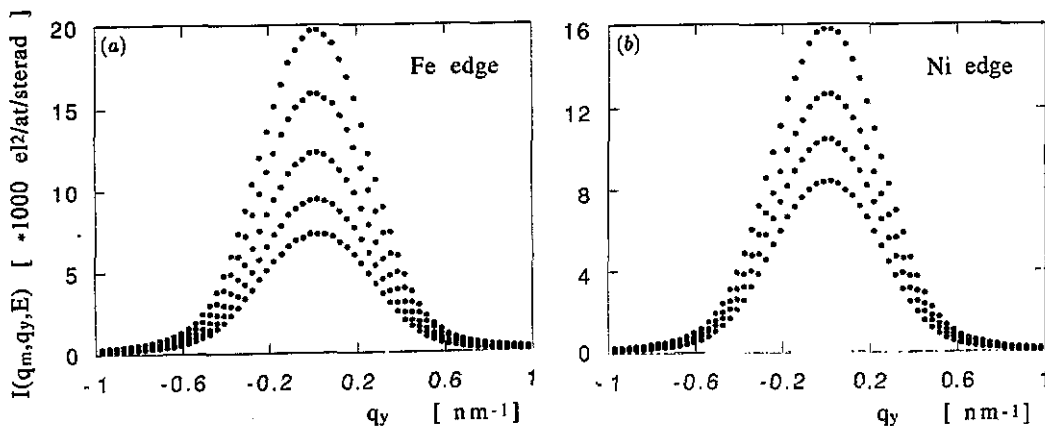

Figure 5. Dependence of the anomalous scattering intensity on the wavevector q_y along the $[q_m, q_y, 0]^*$ segment of the $(001)^*$ reciprocal plane (MY): (*a*) near the Fe edge (7112 eV), where, from top to bottom, the curves correspond to 7104, 7090, 7056, 6990 and 6875 eV; (*b*) near the Ni edge (8333 eV), where, from top to bottom, the curves correspond to 8322, 8310, 8295 and 8250 eV.

OX and MY directions (figures 6(*a*) and 6(*b*)), the maximum for S_{NiNi} is only slightly higher than that for S_{CuCu}, whereas S_{FeFe} is smaller by a factor of more than 2. S_{FeNi} is strongly negative. For the direction OB (figure 6(*c*)), the order of S_{CuCu} and S_{NiNi} reverses. S_{FeFe} is still much smaller than S_{NiNi}, and S_{FeNi} is closer to zero at all wavenumbers. Finally, in the direction OC (figure 6(*d*)), at 45°, S_{CuCu} is much larger than S_{NiNi}, and the sign of S_{FeNi} is now positive. The PSFs in the direction OB have relative amplitudes intermediate between those along OX and OC. As to the position of these maxima, that of Cu–Cu is always slightly smaller than that of Fe–Fe or that of Ni–Ni (which have almost the same value) for a given orientation, and they decrease monotonically with increasing angle α, as was observed for the experimental scattering profiles themselves.
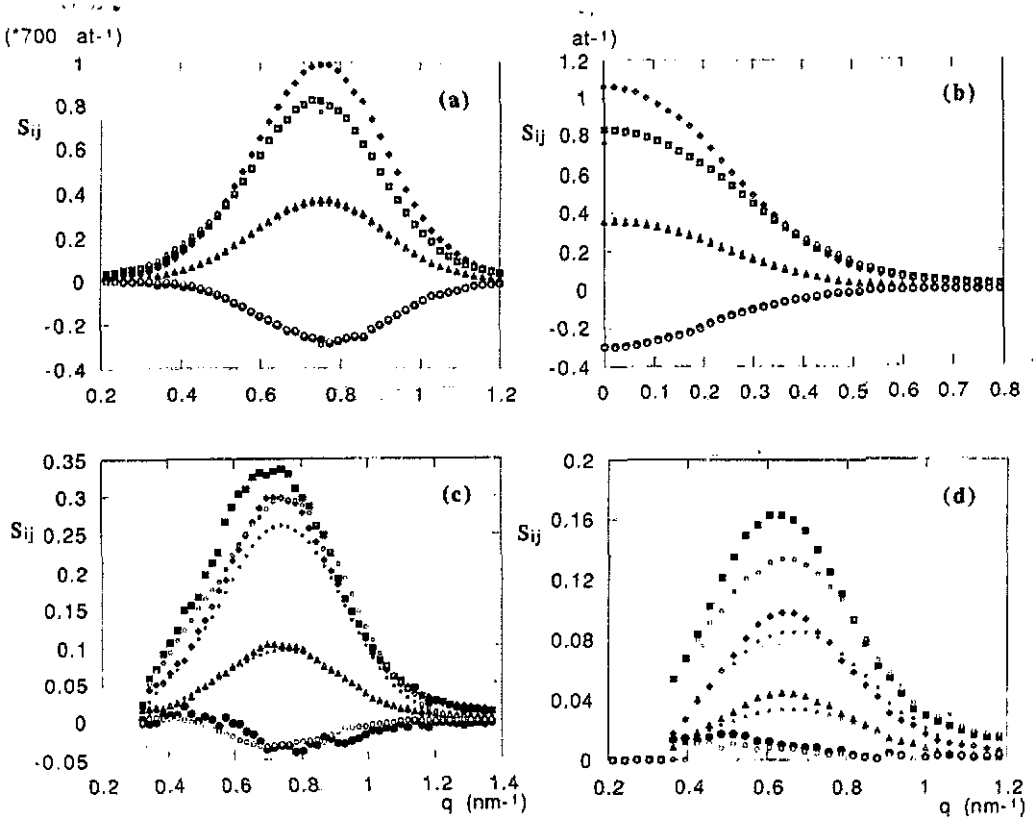
Figure 6. Experimental PSFs (■, ♦, ▲, ●) and PSFs from model predictions (□, ◊, △, ○) in the (*a*) OX, (*b*) MY, (*c*) OB and (*d*) OC directions of the (001)* plane: ■, □, S_{CuCu}; ♦, ◊, S_{NiNi}; ▲, △S_{FeFe}; ●, ○S_{FeNi}.

5. PSF analysis

In order to explain the strong anisotropy of the SAXS profiles and of the PSFs with the sample orientation, we must start by examining the pattern formed during the ageing treatment. We know (cf section 1) that the phase separation produces a fine pattern of three families of irregular platelets lying in the {100} planes. These platelets are alternately enriched in Cu or in Ni–Fe. Since the PSFs are the Fourier transforms of the corresponding real-space pair correlation functions, the presence of thin platelets orthogonal to a ⟨100⟩ direction can explain the strong SAXS intensity along these directions. Since the thickness of the platelets is much less than their width, the correlation between platelets is much stronger in the direction orthogonal to the plane of the platelets than in the two other directions, parallel to the platelets. Each family of platelets can be constructed from irregularly stacked rows along one ⟨100⟩ direction and the correlation between rows or between families is not important. Since the bulk alloy composition is at the centre of the miscibility gap, such a pattern satisfies the condition that it should be space filling by an equal volume fraction of the Cu-rich and the Ni–Fe-rich phases with the same pattern; the Cu-rich platelets and the Ni–Fe-rich platelets with the same average thicknesses alternate in the pile-up. In the ideal case of platelets of equal widths and identically centred, the correlation functions and, consequently, their Fourier transform can be equated to the product

of two terms: the first, $T(q_x)$, depends on q_x along $\langle 100 \rangle^*$ for the pile-up along [100], while the second, $P(q_y, q_z)$, depends on q_y and q_z.

This two-phase model would be sufficient to describe the scattering at a single energy. In that case, the resulting PSFs would be proportional to each other in ratios such that $S_{\text{FeNi}}^2 = S_{\text{FeFe}} S_{\text{NiNi}}$ is obeyed. However, when anomalous scattering is performed, this description fails in two ways.

(i) The ratios of experimental PSFs do not fulfil the relation above, as already noted for polycrystals (I).

(ii) The ratios depend on the scattering direction since S_{FeNi} changes sign between $[100]^*$ and $[110]^*$.

To deal with the first discrepancy, it has been shown in the isotropic case for polycrystals (II) that each PSF S_{ii} ($i \equiv$ Fe, Ni, Cu) can be decomposed into weighted linear combinations of a two-phase term S_a and a correction term S_b:

$$S_{ii}(q) = X_i S_a(q) + Y_i S_b(q). \tag{4}$$

The solute conservation implies that the weights X_i and Y_i can be chosen as

$$
\begin{aligned}
X_{\text{Fe}} &= Y_{\text{Fe}} = 1 \qquad X_{\text{Ni}} = X^2 \qquad Y_{\text{Ni}} = Y^2 \\
X_{\text{Cu}} &= (1 + X)^2 \qquad Y_{\text{Cu}} = (1 + Y)^2.
\end{aligned} \tag{5}
$$

In the two-phase model, X would be equal to the tie-line slope $(C_{\text{Ni},2} - C_{\text{Ni},1})/(C_{\text{Fe},2} - C_{\text{Fe},1})$ where $C_{i,1}$ and $C_{i,2}$ are the concentrations in the two coexisting phases. The weights X and Y must differ, as otherwise equation (4) reverts to the equation for a two-phase model. So Y may be called a pseudo-tie-line slope. Applying to the PSFs along OX, MY, OB or OC the same analysis procedure as in polycrystals gives fairly constant values of X and Y ($\Delta X/X$ or $\Delta Y/Y = \pm 15\%$). These direction-independent tie-line slopes X and Y are close to those computed for polycrystals (II).

For the anisotropic pattern (point (ii) above), using the two terms $T(q_x)$ and $P(q_y, q_z)$ introduced above, we now express S_a and S_b by the products

$$S_a = T_a P_a \tag{6a}$$

$$S_b = T_b P_b. \tag{6b}$$

Taking into account the symmetry between the {001} families, the (001) pile-ups will not contribute to SAXS, since OZ is perpendicular to the scattering plane. Using the notation $S_{ii}(q_x, q_y)$ for the ii PSF at q_x and q_y in reciprocal space, equation (4) becomes

$$
\begin{aligned}
S_{ii}(q_x, q_y) = {}&X_i[T_a(q_x)P_a(q_y) + T_a(q_y)P_a(q_x)] \\
&+ Y_i[T_b(q_x)P_b(q_y) + T_b(q_y)P_b(q_x)].
\end{aligned} \tag{7}
$$

To resolve the parameters introduced in equation (7), a lattice of 50×50 points was defined in the (q_x, q_y) plane. The three sets of three PSFs (directions OX, MY and OC) corresponding to $S_{ii}(q_x, 0)$, $S_{ii}(q_m, q_y)$ and $S_{ii}(q_x, q_x)$ were linearly interpolated on this mesh. Discrete values of T_a, P_a, T_b, P_b, X and Y were then

computed on this lattice to determine the parameters by a least-squares fit procedure. As displayed in equation (7), the fitting parameters X and Y are independent of the lattice points. The X- and Y-values are respectively 1.5 and -1.75 with a relative uncertainty of about 20%. Since the products $T_a P_a$ and $T_b P_b$ cannot be resolved, the P_a and P_b functions were normalized to unity at $q = 0$. The best-fit values obtained for T_a and T_b are shown in figure 7(a) and those for P_a and P_b are shown in figure 7(b). The PSFs calculated using equation (7) were shown in figure 6 together with the experimental PSFs. There is hardly any difference between experimental and calculated PSFs along $\langle 100 \rangle^*$ and $\langle 010 \rangle^*$ (OX and MY). However, the model increasingly underestimates the PSFs as the observation angle α increases (OB and OC). This shortcoming cannot be attributed to the low-intensity PSFs along OB and OC since the intensities were renormalized for the computation of the goodness-of-fit estimator. A refinement of the model is offered in the last paragraph.
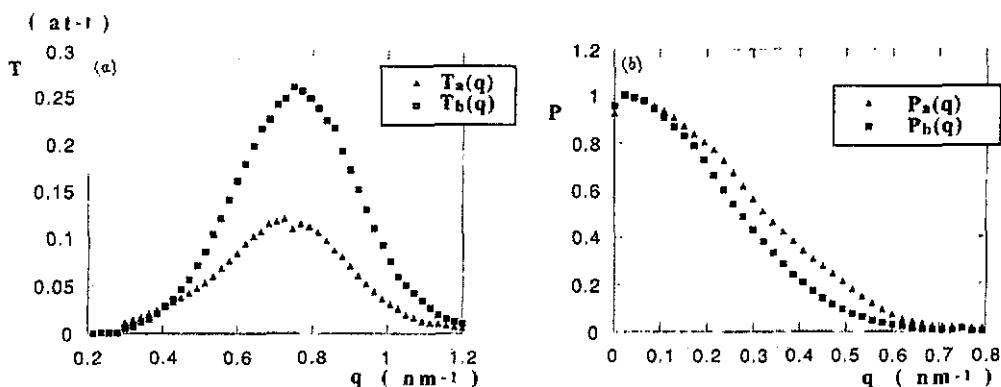

Figure 7. Best decomposition of the experimental PSFs in a (001) pile-up of platelets (notation as in the text).

If we recall that the direction-independent tie-line slopes X and Y are close to those computed using equation (4) in the isotropic case for polycrystals (II), we can explain why X_i and Y_i were invariant in polycrystals although the ratios of $S_a(q)$ to $S_b(q)$ differed greatly from one sample to another. The space-averaged values of $\langle S_a \rangle$ and $\langle S_b \rangle$ depend on texture; however, for $S_{ii}(q)$ for polycrystals expressed as $X_i \langle S_a \rangle + Y_i \langle S_b \rangle$, the X_i and Y_i are independent of the sample texture. Moreover, for a polycrystalline sample ($Cu_{0.425}Ni_{0.425}Fe_{0.15}$ aged for 56 h at 500 °C) measured in earlier synchrotron work (I and unpublished results), we have found variations in the PSF intensities in excess of the relative uncertainty; this is probably due to measurements at different locations in the foil where the texture is not exactly the same.

The factors $T_a(q)$ and $T_b(q)$ (equation (6)) perpendicular to the platelets both have fairly symmetrical humps with identical shapes (figure 7(a)). The maximum of T_b is about twice that of T_a and is almost located at the same q (0.74 nm^{-1} and 0.76 nm^{-1}, respectively). The small q displacement in the maxima agrees with the differing q for the maxima of the PSFs observed in figure 6. The local periodicity in the platelet pile-up along the $\langle 100 \rangle^*$ direction with the repetition distance denoted as R allows one to write the straightforward relation $q_m R \cong 2\pi$ where q_m is the position of the maximum along OX. The resulting values of R are 8.2 nm and 8.5 nm

and the mean platelet thicknesses 4.1 nm and 4.25 nm. The Guinier radii (3.5 nm and 3.6 nm) are not very significant; the scattering halo resulting from the strong correlation between the domains allows a determination only in a q-range beyond its validity limit. Finally, if the two functions T_a and T_b (after normalization of their maxima) are replotted as a function of q/q_m, the resulting profiles are almost identical (figure 8(a)).
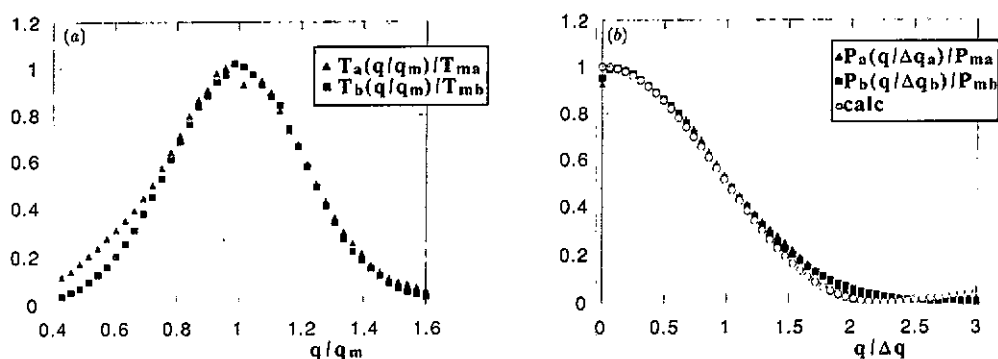

Figure 8. Rescaling of (a) T_a, T_b and (b) P_a, P_b where q_m is the wavenumber of the maxima T_{ma} and T_{mb} along OX and Δq is the HWHM of P_a and P_b along OY.

In figure 7(b), the functions $P_a(q)$ and $P_b(q)$ are not identical. However, when replotted with respect to $q/\Delta q$ (where Δq is the half-width at half-maximum (HWHM) along OY with values of 0.32 nm^{-1} and 0.27 nm^{-1}, respectively), the resulting curves also overlap (figure 8(b)). The rescaled P_a and P_b compare well with the structure factor of a single platelet, i.e. $[\sin^2(qR)]/(qR)^2$ (open symbols). This expression is consistent with the assumption made in the pile-up model that interplatelet correlations are negligible outside the $\langle 100 \rangle$ pile-up directions. The diameters of these platelets, derived from the HWHM, are 8.7 nm and 10.3 nm for P_a and P_b, respectively. This suggests a length-to-thickness ratio of about two, which is somewhat smaller than observed by TEM or FIM.

Equation (7) was also used to reconstruct the isointensity map with the best-fit T_a, T_b, P_a and P_b (figure 3(b)). When compared with the experimental contours (figure 3(a)), it is obvious that the same general trends are reproduced; the strong wide spots are separated by a saddle valley along the $\langle 110 \rangle^*$ direction.

Figure 3(b) also shows that the saddle points along $\langle 110 \rangle^*$ are slightly too low since they lie between the isocontours 0.1 and 0.133 instead of 0.166. This was also illustrated by the open symbols in figure 6(c) which were all lower than the full symbols for the experimental PSFs. The model can be further refined to eliminate this discrepancy by recalling the somewhat wavy tweed pattern observed by TEM and approximating it by a long-wavelength sine wave to ensure slow variation in the platelet orientation. With this additional qualitative assumption, the experimental isointensity map can be reproduced with a greater accuracy. However, at this stage it should not be overlooked that experimental scattering patterns and real-space morphologies are not in one-to-one correspondence.

6. Conclusions

The anisotropic SAXS has been measured on a single crystal of $Cu_{0.44}Ni_{0.42}Fe_{0.14}$

aged for 4 h at 550 °C. It comprises a scattering ring, of which the position of the maximum decreases slightly (15%) from $[100]^*$ to $[110]^*$, but with an intensity which strongly decreases by a factor of more than 5.

The anomalous SAXS measurements show that, in a given direction, the PSFs have almost the same shape, but the intensity ratio between PSFs changes with direction; for instance, S_{FeNi} changes from negative to positive values when one moves from the $[100]^*$ to the $[\bar{1}10]^*$ direction.

We have shown that the PSFs can be decomposed into a sum of two terms, S_a and S_b, of almost the same shape; this indicates that S_a and S_b correspond to patterns with almost the same short-range periodicities. The relative ratio of S_a to S_b varies markedly as the direction changes from $\langle 100 \rangle^*$ to $\langle 110 \rangle^*$. Independently of the scattering direction, the two-phase term S_a has a tie-line slope X of 1.5 and the correction term S_b has a pseudo-tie-line slope Y of -1.75. These values are close to those previously obtained for polycrystals (II). This new result thus sheds light on the fact that both slopes had rather invariant values in our work on polycrystals despite the fact that the ratio of S_a to S_b varied from one sample to another (owing to differences in the texture).

An anisotropic model of platelet pile-up has been introduced on the basis of FIM images (Wagner *et al* 1984) and TEM observations (Wahi and Stajer 1984). We modelled the tweed pattern by an alternating pile-up of equal-thickness platelets of a Cu-rich and an Ni–Fe-rich phase. This model reproduces the detailed features of the anisotropic SAXS.

The most unexpected result from this model is that, along the pile-up direction, the correction term S_b is larger than the two-phase term S_a by a factor of 2 while, on the contrary, S_b is weaker than S_a in the in-platelet direction. In the context of the physical interpretation given in II for the term S_b, namely that this term is due to a local segregation of Fe at the interfaces between Cu and Ni–Fe phases, this would mean that pronounced segregation is taking place, perhaps extending to several planes. The interfacial segregation in the $\{100\}$ coherency planes gives a contribution stronger than the two-phase pattern.

To further this study, samples at different stages of phase decomposition are being examined. The systematic variation in platelet size and anisotropy should yield a better understanding of the inadequacy of the two-phase model to describe the PSFs in this paper. Alternative descriptions of the PSF profiles is also being investigated.

Acknowledgments

Appendix

We recall equation (3):

$$I_k(q, E_k) = \sum_i A_i(E_k) \cdot S_{ii}(q)$$

where the brackets have been dropped. After normalization of the vector $A(E)$, one obtains

$$J_k(E_k) = \sum_{q_1}^{q_2} \frac{I_k(q, E_k)}{|A(E_k)|} = B(E_k) \cdot \sum_{q_1}^{q_2} S_{ij}(q) \tag{A1}$$

which we rewrite for brevity as

$$J_k = B_k \cdot S.$$

Since this system of equations is rather ill conditioned even when data are recorded on two edges, this means that it is completely singular on a single edge. This implies that the B_k vectors are all orthogonal to the same vector N_w in the orthonormal 3D space based on S_{11}, S_{12} and S_{22}. N_w depends on the edge selected. Then we can write

$$B_k \cdot N_w \simeq 0 \qquad \text{with } N_w = (N_x, N_y, N_z). \tag{A2}$$

The coordinates of N_w can be determined by minimization of the following norm with respect to N_x and N_y:

$$\frac{1}{n} \sum_k (B_k^x N_x + B_k^y N_y + B_k^z N_z)^2. \tag{A3}$$

The next step consists of changing the set of orthogonal vectors from (X, Y, Z) to (N_u, N_v, N_w) with the following conditions: $N_u = \overline{B_k}$, $N_v = N_w \times N_u$. With this new set of orthogonal vectors, the unknown vector and the vectors B_k can be written as

$$S = S_u N_u + S_v N_v + S_w N_w \qquad B_k = B_u^k N_u + B_v^k N_v + B_w^k N_w \tag{A4}$$

and, since B_w^k is almost equal to 0, the set of equations becomes

$$J_k = B_k \cdot S = S_u B_u^k + S_v B_v^k. \tag{A5}$$

This means that, in the N_w plane, the straight lines defined by the last equation should cross at the same point. This can be checked on a plot, and one can disregard any bad data far from the common trend, after which the solution is calculated by a least-squares method. The figure of merit is defined as the relative dispersion of the crossing point of the data divided by the distance from the origin to the crossing point, for the selected energies. This operation is done on the two sets of data, the two edges being processed separately.

We are then left with two vectors S^i with unknown components S_w^i and we have to define a condition of compatibility of the data between both edges. Rewriting the S^i as $S^i = S_u^i N_u^i + S_v^i N_v^i + S_w^i N_w^i = E^i + S_w^i N_w^i$, $i = 1, 2$, and defining $V = N_w^1 \times N_w^2$, the intersection between the two planes, it follows that

$$\lambda = V \cdot E^1 / V \cdot E^2 \cong 1. \tag{A6}$$

This last relation gives a compatibility condition for the data between the two edges. If it is not fulfilled, it implies either that the data have been incorrectly selected or that there is a serious normalization problem between the two edges. In any case the resulting solution should be regarded with utmost suspicion. It is to be noted that this number λ, coming from the ratio of the scalar products of the vectors E and V (equation (A6)) which are almost orthogonal, is very sensitive to errors in E.

The last unknown is then determined by the following equation:

$$S_w^1 = (-E^1 \cdot E^2 + \lambda E^2 \cdot E^2)/E^2 \cdot N_w^1. \tag{A7}$$

References

Binder K 1991 *Materials Science and Technology vol 5 Phase Transformations in Materials* (Weinheim: VCH)
Chart T G, Gohil D H and Shu X Z 1982 *National Physical Laboratory, Teddington, Middx, Report* DMA (A) 54
Furukawa H 1985 *Adv. Phys.* **34** 703
Guilarducci de Salva A, Simon J P, Livet F and Guyot P 1987 *Scr. Metall.* **21** 1061
Hoyt J J 1989 *Acta Metall.* **37** 2489
—— 1990 *Acta Metall.* **38** 227
Kostorz G 1991 *J. Appl. Crystallogr.* **24** 444
Lyon O and Simon J P 1987 *Phys. Rev.* B **35** 5164
—— 1988 *J. Phys. F: Met. Phys.* **18** 1787
Piller J, Wagner W, Wollenberger H and Mertens P 1984 *Decomposition of Alloys: The Early States* ed P Haasen *et al* (Oxford: Pergamon) p 156
Wagner W, Poerschke R and Wollenberger H 1984 *Decomposition of Alloys: The Early States* ed P Haasen *et al* (Oxford: Pergamon) p 170
Wahi R P and Stajer J 1984 *Decomposition of Alloys: The Early States* ed P Haasen *et al* (Oxford: Pergamon) p 165